Transport and thermoelectric properties of the $LaAlO_3/SrTiO_3$ interface

A. Jost, V. K. Guduru, S. Wiedmann, J. C. Maan, and U. Zeitler*
High Field Magnet Laboratory, Institute for Molecules and Materials, Radboud University Nijmegen, Toernooiveld 7, 6525ED Nijmegen, The Netherlands

S. Wenderich, A. Brinkman, and H. Hilgenkamp
Faculty of Science and Technology and MESA+ Institute for Nanotechnology, University of Twente, 7500AE Enschede, The Netherlands

(Received 28 July 2014; revised manuscript received 12 December 2014; published 26 January 2015)

The transport and thermoelectric properties of the interface between $SrTiO_3$ and a 26-monolayer-thick $LaAlO_3$ layer grown at high oxygen pressure have been investigated at temperatures from 4.2 to 100 K and in magnetic fields up to 18 T. For $T > 4.2$ K, two different electronlike charge carriers originating from two electron channels which contribute to transport are observed. We probe the contributions of a degenerate and a nondegenerate band to the thermoelectric power and develop a consistent model to describe the temperature dependence of the thermoelectric tensor. Anomalies in the data point to an additional magnetic field dependent scattering.

DOI: 10.1103/PhysRevB.91.045304 PACS number(s): 73.40.−c, 72.15.Jf

I. INTRODUCTION

Since the discovery of conduction at the interface between the two band-insulating perovskite oxides $SrTiO_3$ (STO) and $LaAlO_3$ (LAO) [1] a plethora of new effects have been found, ranging from superconductivity [2] to magnetism [3–10] and tunable switching of high mobility interface conductivity [11–13], depending on the ground state the sample reaches. The nature of the ground state present in the systems depends closely on the growth parameters of the $LaAlO_3$ layer [3], the $LaAlO_3$ layer thickness [14–16], and the configuration of the heterostructures with different capping layers on top of $LaAlO_3$ [10,17–19].

A number of possible mechanisms are proposed to be responsible for the conduction at the interface [20–25], which can lead to multiple charge-carrier conduction if several are active. Indeed multiple carrier conduction has been found in $SrTiO_3/LaAlO_3$ interfaces over a wide range of growth conditions [4,17,26–30].

Until the present, most investigations on the electronic properties of $LaAlO_3/SrTiO_3$ interfaces have been done using transport experiments [1–19,26,29–32], while measurements of thermoelectric power are still sparse in $SrTiO_3/LaAlO_3$ interfaces [28,33,34]. Whereas transport experiments are generally dominated by the charge-carrier mobility, contributions of lower mobility can be accessed in thermoelectric power measurements. Additionally, the thermoelectric power is known to be sensitive to magnetic scattering, and thus is an ideal tool to investigate multiple charge-carrier contributions in samples with magnetic signatures.

In the present work we report on our investigation of the interface electronic structure of one specific type of LAO/STO heterostructure, with a 10-nm (26 unit cells) LAO film, which is known to exhibit magnetic signatures [3]. Magnetotransport and thermoelectric-power measurements have been performed in a large temperature and magnetic field range. We apply a two carrier model to the magnetotransport data and find two different charge carriers with different densities and mobilities. By combining transport and thermopower data, we extend this model to the thermoelectric tensor ϵ at zero field and develop a preliminary description for its behavior in magnetic field.

The paper is organized as follows: in Sec. II we describe the details of sample growth and the experimental setup. In Sec. III we show our transport results, which we describe in terms of a classical two-carrier model. In Sec. IV we present our results of the thermopower measurements and extend our model to thermopower. In Sec. V we discuss our results and draw conclusions in Sec. VI.

II. EXPERIMENTAL DETAILS

The sample is grown by pulsed laser deposition and has a 10-nm-thick (26 unit cells) LAO film on a TiO_2-terminated single-crystal STO [001] substrate (treatment described in Ref. [35]). The LAO film was deposited at a substrate temperature of 850 °C and an oxygen pressure of 2×10^{-3} mbar, in order to minimize oxygen vacancies, using a single-crystal $LaAlO_3$ target. The growth of the LAO film was monitored using *in situ* reflection high-energy electron diffraction. After the growth, the samples were cooled to room temperature at the deposition pressure.

Electrical contacts to the sample were made using an ultrasonic wire bonder to punch through the LAO layers and attaching manganine wires to the holes with silver paint.

The thermoelectric power was measured in a home-built apparatus in a standard one heater, two thermometer geometry similar to the one used in Ref. [36]. The resistivity was measured on the same sample and in the same apparatus using a conventional low-noise lock-in technique. Both quantities were measured in positive and negative field directions and the data shown are symmetrized (antisymmetrized) to obtain the diagonal (off-diagonal) components of the resistivity- and thermoelectric power tensors. We use the historical sign convention for the Nernst-Ettingshausen effect throughout the paper (positive Nernst signal along the y direction, when the field is in the z direction and the gradient is in the x direction).

*u.zeitler@science.ru.nl

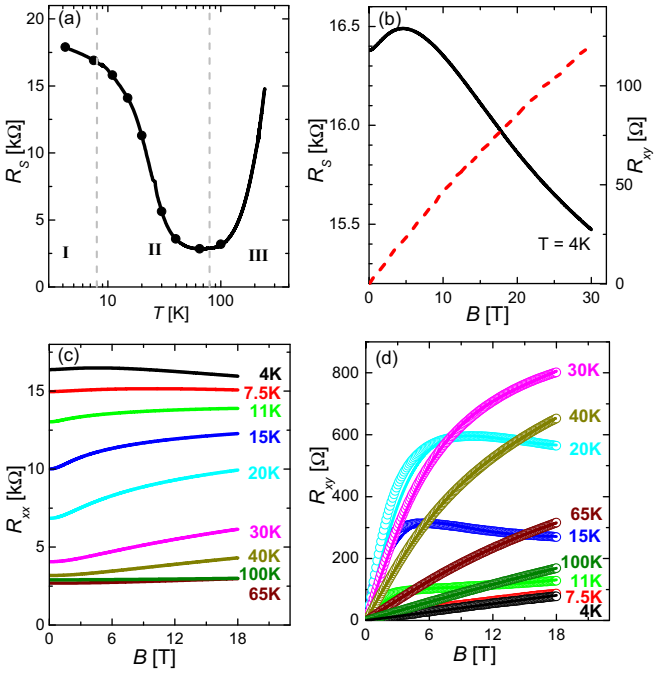

FIG. 1. (Color online) (a) Temperature dependence of sheet resistance (line). Sheet resistance from the two-charge-carrier model (dots). (b) Sheet resistance (black line) and Hall resistance (dashed red line) at 4 K showing the negative magnetoresistance and the linear Hall effect. (c) Measured sheet resistance R_{xx} for temperature between 4 and 100 K. (d) Measured Hall resistivity for temperature between 4 and 100 K (empty dots). Fits with the two-charge-carrier model (lines).

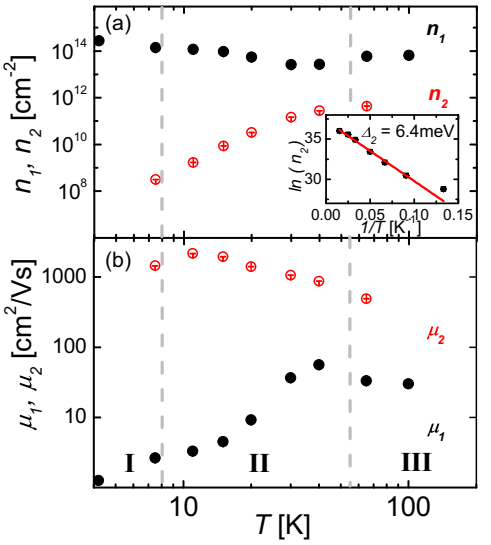

FIG. 2. (Color online) (a) Charge-carrier densities of the two electronlike bands n_1, n_2 from the two-charge-carrier model (inset: Arrhenuis plot for n_2). (b) Mobilities of the two electronlike bands μ_1, μ_2 from the two-charge-carrier model.

III. MAGNETOTRANSPORT

The temperature dependence of the sheet resistance R_S, the magnetoresistance R_{xx}, and the Hall data R_{xy} are shown in Figs. 1(a), 1(c), and 1(d), respectively. The analysis of the transport data follows closely our previous work [26]. From the transport data (Fig. 1), we can distinguish three different regions (from low to high temperature): region I (up to ∼8 K) with logarithmically decreasing sheet resistance and linear Hall effect, region II (∼8 to ∼50 K) with strongly decreasing sheet resistance and strongly nonlinear Hall resistance, and region III (above ∼50 K) showing an increase in the sheet resistance and a linear Hall effect with respect to the magnetic field.

The transport data can be analyzed using a two-charge-carrier model for two independent, electronlike channels. For $T > 7.5$ K the magnetic field dependent Hall resistance R_{xy} was fitted with a restriction to the zero-field resistance R_{S0} using the equations [37]

$$R_{xy} = \frac{B}{e}\frac{\left(n_1\mu_1^2 + n_2\mu_2^2\right) + (\mu_1\mu_2 B)^2(n_1+n_2)}{(n_1\mu_1 + n_2\mu_2)^2 + (\mu_1\mu_2 B)^2(n_1+n_2)^2},$$
$$R_{S0} = \frac{1}{e(n_1\mu_1 + n_2\mu_2)}, \quad (1)$$

with e the electron charge, B the magnetic field, and the independent fitting parameters $n_{1,2}$ and $\mu_{1,2}$ as charge-carrier density and mobility for the two channels, respectively. For the lowest and highest temperature, where the Hall resistance is completely linear, the density for one type of charge carrier was obtained from a linear fit to $R_{xy} = B/(en)$ and the mobility from $R_{S0} = 1/(en\mu)$. The obtained fitting parameters are shown in Fig. 2 [38]. The first type of charge carriers (n_1, μ_1) has a relatively high and temperature-independent charge-carrier density of about $n_1 \sim 10^{14}\,\mathrm{cm}^{-2}$. The mobility of these charge carriers is low with $\mu_1 \sim 40\,\mathrm{cm}^2/\mathrm{V\,s}$ and decreases towards lower temperatures to $\mu_1 \sim 1\,\mathrm{cm}^2/\mathrm{V\,s}$ at 4 K (therefore referred to as low mobility charge carriers). This decrease in mobility to lower temperatures was attributed to magnetic, Kondo-like scattering due to the negative magnetoresistance at low temperatures and is described in more detail in our previous work [3,26]. The slight decrease in mobility at higher temperatures is probably due to electron-phonon scattering.

The second type of charge carriers has a much lower charge-carrier density, which is increasing with a thermally activated behavior $n_2 \propto e^{-\Delta_2/k_BT}$ from $n_2 \sim 2\times10^9\,\mathrm{cm}^{-2}$ at 11 K to $n_2 \sim 4\times10^{11}\,\mathrm{cm}^{-2}$ at 65 K; i.e., we deal with charge carriers, which have to be treated as a nondegenerate electron gas. To derive the energy gap between the nondegenerate, high mobility band at higher energy and the low-lying, low mobility band, we can use an Arrhenius plot [inset of Fig. 2(a)], which gives a gap of $\Delta_2 = (6.4 \pm 0.4)\,\mathrm{meV}$, comparable to the results on other samples [10,19,26]. The mobility is high at low temperatures ($\mu_2 \sim 2000\,\mathrm{cm}^2/\mathrm{V\ s}$) and decreases at higher temperatures by one order of magnitude (high mobility charge carriers).

IV. THERMOELECTRIC POWER

The temperature dependence of the zero-field thermoelectric power $-S_{xx}$ is shown in Fig. 3(a). First, the thermoelectric power is negative, confirming that our carriers are electrons. Second, we point out the absence of a clear phonon-drag peak

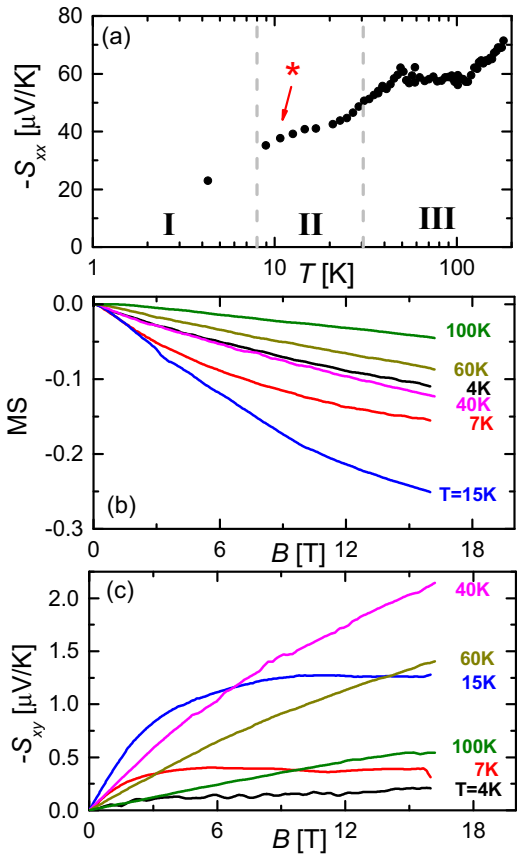

FIG. 3. (Color online) (a) Zero-field thermoelectric power S_{xx} in a semilogarithmic plot for clarity. A small deviation from the observed $T^{0.4}$ dependence around 15 K is marked by an asterisk. (b) Magnetothermopower MS (see text) for selected temperatures. (c) Nernst effect S_{xy} for selected temperatures.

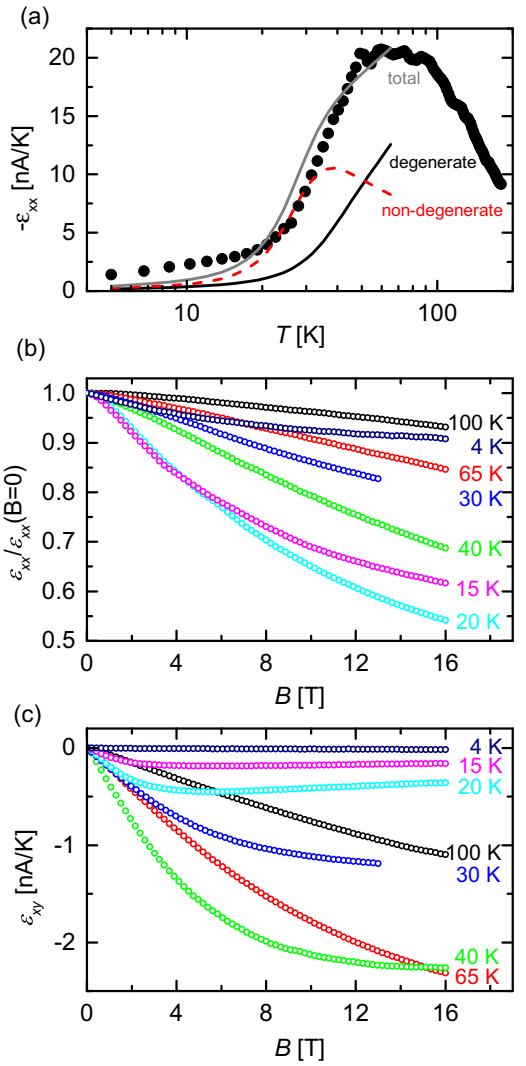

FIG. 4. (Color online) (a) Temperature dependence of ϵ_{xx} (black dots). For illustration typical curves for degenerate and nondegenerate electrons are shown (see text). (b) Magnetic field dependence of ϵ_{xx} for selected temperatures between 4 and 100 K. (c) Magnetic field dependence of ϵ_{xy} for selected temperatures between 4 and 100 K.

[36]. Only a faint deviation from the observed dependence is visible around 15 K (marked by an asterisk). Thus we assume that we are in the regime of diffusion-dominated thermopower. The three regions identified in the transport measurements are indicated by the dashed lines. Region I cannot be clearly identified in thermopower due to the lack of data points. In region II, the thermopower is increasing monotonously, proportional to approximately $T^{0.3}$–$T^{0.4}$. We note that the temperature dependence is also in agreement with thermoelectric power by variable range hopping which gives a $T^{1/3}$ dependence for a two-dimensional (2D) electron gas [39].

If multiple charge carriers are present, the individual contributions of the charge carrier have to be weighted by their conductivities and we can write for S_{xx} at zero magnetic field [40]

$$S_{xx} = \frac{\sigma_{xx}^{(1)} S_{xx}^{(1)} + \sigma_{xx}^{(2)} S_{xx}^{(2)}}{\sigma_{xx}^{(1)} + \sigma_{xx}^{(2)}}. \quad (2)$$

The combination of both contributions explains the observed temperature dependence and will be described later in this paper using the thermoelectric tensor (see Fig. 4).

In region III, the thermopower is constant up to about 120 K and increases monotonously at higher temperatures, again proportional to approximately $T^{0.4}$.

When a magnetic field is applied, the magnitude of the thermoelectric power decreases. We can define the magnetothermopower MS as

$$MS(B) = \frac{S_{xx}(B) - S_{xx}(B=0)}{S_{xx}(B=0)}, \quad (3)$$

shown in Fig. 3(b). In region I (4 K), the magnetothermopower is weak and linear with a decrease by about 11% at 16 T. In region II, the MS becomes stronger and nonlinear with a maximal suppression of 25% at 15 K. Above 15 K the magnetothermopower becomes weaker again but remains nonlinear. In region III, the magnetothermopower is reduced even more and becomes linear again.

The Nernst effect S_{xy} [Fig. 3(c)] shows similar behavior. In region I it is nearly linear and small, with

$\nu = S_{xy}/B \approx -12\,\mathrm{nV/(TK)}$. We note that this is still enhanced compared to the classical Fermi-liquid picture [41], which is approximately

$$\nu = -\frac{\pi^2}{3}\frac{k_B}{e}\frac{k_B T}{\epsilon_F}\mu \approx -[0.1\ldots 1]\frac{\mathrm{nV}}{\mathrm{TK}} \tag{4}$$

depending on the actual Fermi energy. At higher temperature (region II), S_{xy} becomes nonlinear and increases by an order of magnitude at 40 K and 16 T in comparison to the value at 4 K. When entering region III, the Nernst signal becomes linear again and decreases toward higher temperatures.

The overall behavior of the thermoelectric signals in magnetic field resembles the transport signals, i.e., linear and small in regions I and III and nonlinear and large in region II. It is therefore beneficial to derive an appropriate two-charge-carrier model for the thermopower, which can be done following the work of Cao *et al.* [42].

The thermopower tensor is defined by $S = E/(\nabla T)$ under the condition of $J_q = 0$, with E the electric field, J_q the charge current density, and ∇T the temperature gradient. We can use an extended Ohm's law

$$J_q = \sigma E - \epsilon \nabla T, \tag{5}$$

with σ the conductivity tensor, ϵ the thermoelectric tensor, and $\rho = \sigma^{-1}$ the resistivity, to find an expression for the thermopower tensor:

$$S = E/(\nabla T) = \sigma^{-1}\epsilon = \rho\epsilon. \tag{6}$$

By rewriting Eq. (6), we get $\epsilon = \sigma S$ for the thermoelectric tensor. Using σ and S from our measured data we obtain ϵ_{xx} and ϵ_{xy}, shown in Fig. 4.

The temperature dependence of the thermoelectric tensor ϵ_{xx} at zero magnetic field [Fig. 4(a)] is characterized by a negative quantity (typical for electrons), the magnitude of which increases linearly with temperature for $T < 25$ K. At 25 K, the thermoelectric tensor starts to increase rapidly up to a plateau, which extends between 50 and 90 K. This increase originates from two simultaneous effects: the increase in mobility of the low mobility (degenerate) charge carriers and the thermally activated population of the high mobility (nondegenerate) band. Above 90 K, the thermoelectric tensor starts to decrease, probably due to an increase in phonon scattering.

To describe the zero-field data, the contributions of the degenerate and the nondegenerate band have to be added up: $\epsilon = \epsilon_d + \epsilon_{nd}$. The degenerate, low mobility band can be described by the well-known Mott formula [43]:

$$\epsilon_d = -\sigma_d \frac{\pi^2 k_B}{3e}\frac{k_B T}{\epsilon_F}(1+p), \tag{7}$$

with the Fermi energy ϵ_F and the scatter parameter $p = (\partial ln\,\tau/\partial ln\,\varepsilon)|_{\varepsilon_F}$. The temperature dependence of the thermopower of a nondegenerate two-dimensional electron gas (as are the thermally excited high mobility charge carriers) is given by [44]

$$\epsilon_{nd} = \sigma_{nd}\frac{k}{e}\left[(p+2) + \frac{\epsilon_e}{kT}\right], \tag{8}$$

with ϵ_e the Fermi energy measured from the lower edge of the conduction band and $p = (\partial ln\,\tau/\partial ln\,\varepsilon)$. Thus, the thermopower of a nondegenerate electron gas is proportional to $1/T$.

To illustrate the behavior of the temperature dependence of these bands, we plotted typical curves for the thermoelectric tensor of degenerate and nondegenerate electron systems ϵ_d and ϵ_{nd} in Fig. 4(a) using the conductivities of the two bands as determined by the transport measurements.

As parameters for the curves we used $p = -0.5$, which is the theoretical value for hard-sphere scattering [45], $\epsilon_e = 6.4$ meV for the nondegenerate gas, as extracted from the thermal activation analysis, and $\epsilon_F = 20$ meV for the degenerate electron gas, in order to achieve the right magnitude compared to the data measured. We note that $\epsilon_F = 20$ meV is in the right order of magnitude for a 2D electron gas with the density measured. Fitting the temperature dependence is not possible because the scatter parameters and energies in Eqs. (7) and (8), respectively, are not independent from each other. The actual values of the scatter parameter $p^{(i)}$ and the energies ϵ_e and ϵ_F can be determined by magnetic field dependent measurements, using an appropriate model for the magnetic field dependence of the two bands.

The magnetic field dependences of the diagonal $[\epsilon_{xx}/\epsilon_{xx}(B=0)]$ and off-diagonal (ϵ_{xy}) components of the thermoelectric tensor are shown in Figs. 4(b) and 4(c), respectively. The magnitude of the diagonal component of the thermoelectric tensor $\epsilon_{xx}/\epsilon_{xx}(B=0)$ decreases with field at all measured temperatures. However, the details of their magnetic field dependences change drastically. At low temperatures, $\epsilon_{xx}/\epsilon_{xx}(B=0)$ decreases steeply at low fields, turning into saturation toward higher fields. The total decrease is thereby the largest at 20 K. Starting from 30 K, $\epsilon_{xx}/\epsilon_{xx}(B=0)$ is flat at low fields, getting steeper toward high fields and saturating again at highest fields. This saturation vanishes at 100 K within the measured field range.

The off-diagonal component ϵ_{xy} increases linearly at low fields, changing with a kink to a lower, still linear slope at higher fields. The field where the slope changes increases linearly with temperature from about 2 T at 4 K to 4.2 T at 20 K. Due to the sharpness of the kink and his B-T dependence, we attribute this kink to be a remnant of magnetic scattering. At 30 and 40 K, a similar change in the slope exists, but at higher fields and smeared out over several Teslas. Therefore, we attribute this behavior to the existence of two different types of charge carriers. At 65 and 100 K, the transition either vanishes or is so much broadened and shifted to higher fields that it is not visible anymore in our measurement.

To model the field dependence of the thermoelectric tensor of the first type of charge carriers, we can use an expression for the diffusion thermoelectric tensor in the classical, degenerate limit given by [36]

$$\begin{aligned}\epsilon_{xx} &= -\sigma_{xx}\frac{L_0 eT}{\varepsilon_F}\left[1 + p\frac{1-\mu^2B^2}{1+\mu^2B^2}\right],\\ \epsilon_{xy} &= -\sigma_{xy}\frac{L_0 eT}{\varepsilon_F}\left[1 + \frac{2p}{1+\mu^2B^2}\right],\end{aligned} \tag{9}$$

with $L_0 = \pi^2 k_B^2/3e^2$ the Lorenz number, k_B the Boltzmann constant, ε_F the Fermi energy, $p = (\partial ln\,\tau/\partial ln\,\varepsilon)|_{\varepsilon_F}$, and τ the transport lifetime. The conductivities σ_{xx} and σ_{xy} are

calculated with

$$\sigma_{xx} = \frac{ne\mu}{1+\mu^2B^2}, \quad \sigma_{xy} = \frac{ne\mu^2B}{1+\mu^2B^2}, \tag{10}$$

using the charge-carrier densities n and the mobilities μ obtained from the transport data (Fig. 2).

The second type of charge carriers (n_1, μ_1) is nondegenerate. Therefore it cannot be modeled with the same equations. To the best of our knowledge, a theoretical model for the magnetic field dependent thermopower of a nondegenerate electron gas is still missing. A development of such a model is beyond the scope of this work and remains as a future challenge.

V. DISCUSSION

The main part of our data, i.e., for temperatures above 30 K, seems to be well described by a two-charge-carrier model, also for thermoelectric power. However, below 30 K some peculiar features are observed: first, the magnitude of the Nernst signal is enhanced compared to the Fermi-liquid picture; second, the kink observed in the off-diagonal component of the thermoelectric tensor ϵ_{xy} has a linear B-T dependence.

A similar anomaly is observed in transport measurements at the same temperature, namely, the observation of a negative magnetoresistance shown in Fig. 1(b) and described elsewhere [3,26]. There, the negative magnetoresistance is attributed to magnetic, Kondo-like scattering. Indeed, the thermoelectric power in Kondo lattices shows similar behavior as in the $LaAlO_3/SrTiO_3$ interface.

In three-dimensional Kondo lattices with one type of charge carrier, the Seebeck coefficient S_{xx} is decreasing strongly with magnetic field and saturating at high fields, and the Nernst coefficient $\nu = S_{xy}/B$ is large at small fields and decreasing to higher fields [46,47]. In other words, the Nernst effect is increasing strongly at low magnet fields and saturates at high fields. In our measurements, we observe the same behavior for low temperatures; a strong decrease in the Seebeck effect with saturation to high fields and a strong increase in Nernst at low field saturating at high fields (see Fig. 3). Since we observe the same signatures as in Kondo-lattice materials, we suggest that a similar mechanism could play a role in our sample and we attribute the strong magnetic field dependence of the thermoelectric tensor to an additional magnetic scattering acting on the low mobility charge carriers (n_1,μ_1) at low temperature.

A possible route to magnetic scattering can be explained by the polar-catastrophe scenario [20], where charge is transferred to the interface due to the polarity of the $LaAlO_3$ layers. This additional charge can change the electric state of the nonmagnetic Ti^{4+} ions in $SrTiO_3$ to magnetic Ti^{3+} ions [9,48]. These magnetic Ti^{3+} ions then can act as scattering partners for the electrons at the interface and the low mobility charge carriers are located close to the interface at the Ti^{3+} ions. Over the location of the high mobility charge carriers we cannot give any conclusion.

We lack an appropriate model to determine the density of magnetic moments at the interface from our data. However, we can place an upper limit by assuming that they are created by the electrons arising from the polar catastrophe. This would give an upper limit of 1/2 a moment per unit cell or $3.4 \times 10^{-14}\,\mathrm{cm}^{-2}$.

VI. CONCLUSION

We have measured a complete set of transport and thermoelectric power data in a temperature range from 4 to 100 K in fields up to 18 T. We find two different electronlike charge carriers with different densities and mobilities: a degenerate band with a low mobility and a high carrier density and a nondegenerate band with a higher mobility, which vanishes at low temperatures. The temperature dependence of the thermoelectric tensor can be described by this two-band picture, but for the magnetic field dependence an appropriate model for the nondegenerate band is still missing. We identify anomalies in the thermopower data, which cannot be readily explained by the two-band picture. We attribute them to an additional strongly magnetic field dependent scattering mechanism of the low mobility charge carriers located close to the Ti^{3+} atoms at the interface.

ACKNOWLEDGMENTS

This work has been performed at the High Field Magnet Laboratory, member of the European Magnetic Field Laboratory, and is part of the InterPhase research program of the Foundation for Fundamental Research on Matter (financially supported by the Netherlands Organization for Scientific Research).

[1] A. Ohtomo and H. Y. Hwang, Nature (London) **427**, 423 (2004).
[2] N. Reyren, S. Thiel, A. D. Caviglia, L. F. Kourkoutis, G. Hammerl, C. Richter, C. W. Schneider, T. Kopp, A.-S. Rüetschi, D. Jaccard, M. Gabay, D. A. Muller, J.-M. Triscone, and J. Mannhart, Science **317**, 1196 (2007).
[3] A. Brinkman, M. Huijben, M. van Zalk, J. Huijben, U. Zeitler, J. C. Maan, W. G. van der Wiel, G. Rijnders, D. H. A. Blank, and H. Hilgenkamp, Nat. Mater. **6**, 493 (2007).
[4] M. Ben Shalom, C. W. Tai, Y. Lereah, M. Sachs, E. Levy, D. Rakhmilevitch, A. Palevski, and Y. Dagan, Phys. Rev. B **80**, 140403 (2009).
[5] Ariando, X. Wang, G. Baskaran, Z. Q. Liu, J. Huijben, J. B. Yi, A. Annadi, A. R. Barman, A. Rusydi, S. Dhar, Y. P. Feng, J. Ding, H. Hilgenkamp, and T. Venkatesan, Nat. Commun. **2**, 188 (2011).
[6] D. A. Dikin, M. Mehta, C. W. Bark, C. M. Folkman, C. B. Eom, and V. Chandrasekhar, Phys. Rev. Lett. **107**, 056802 (2011).
[7] L. Li, C. Richter, J. Mannhart, and R. C. Ashoori, Nat. Phys. **7**, 762 (2011).
[8] J. A. Bert, B. Kalisky, C. Bell, M. Kim, Y. Hikita, H. Y. Hwang, and K. A. Moler, Nat. Phys. **7**, 767 (2011).
[9] J.-S. Lee, Y. W. Xie, H. K. Sato, C. Bell, Y. Hikita, H. Y. Hwang, and C.-C. Kao, Nat. Mater. **12**, 703 (2013).

[10] M. Huijben, G. Rijnders, D. H. A. Blank, S. Bals, S. Van Aert, J. Verbeeck, G. Van Tendeloo, A. Brinkman, and H. Hilgenkamp, Nat. Mater. **5**, 556 (2006).

[11] S. Thiel, G. Hammerl, A. Schmehl, C. W. Schneider, and J. Mannhart, Science **313**, 1942 (2006).

[12] A. D. Caviglia, S. Gariglio, N. Reyren, D. Jaccard, T. Schneider, M. Gabay, S. Thiel, G. Hammerl, J. Mannhart, and J.-M. Triscone, Nature (London) **456**, 624 (2008).

[13] V. K. Guduru, A. Granados del Aguila, S. Wenderich, M. K. Kruize, A. McCollam, P. C. M. Christianen, U. Zeitler, A. Brinkman, G. Rijnders, H. Hilgenkamp, and J. C. Maan, Appl. Phys. Lett. **102**, 051604 (2013).

[14] Y. Kozuka, M. Kim, H. Ohta, Y. Hikita, C. Bell, and H. Y. Hwang, Appl. Phys. Lett. **97**, 222115 (2010).

[15] F. J. Wong, R. V. Chopdekar, and Y. Suzuki, Phys. Rev. B **82**, 165413 (2010).

[16] C. Bell, S. Harashima, Y. Hikita, and H. Y. Hwang, Appl. Phys. Lett. **94**, 222111 (2009).

[17] A. McCollam, S. Wenderich, M. K. Kruize, V. K. Guduru, H. J. A. Molegraaf, M. Huijben, G. Koster, D. H. A. Blank, G. Rijnders, A. Brinkman, H. Hilgenkamp, U. Zeitler, and J. C. Maan, APL Mater. **2**, 022102 (2014).

[18] M. Huijben, A. Brinkman, G. Koster, G. Rijnders, H. Hilgenkamp, and D. H. A. Blank, Adv. Mater. **21**, 1665 (2009).

[19] M. Huijben, G. Koster, M. K. Kruize, S. Wenderich, J. Verbeeck, S. Bals, E. Slooten, B. Shi, H. J. A. Molegraaf, J. E. Kleibeuker, S. van Aert, J. B. Goedkoop, A. Brinkman, D. H. A. Blank, M. S. Golden, G. van Tendeloo, H. Hilgenkamp, and G. Rijnders, Adv. Funct. Mater. **23**, 5240 (2013).

[20] N. Nakagawa, H. Y. Hwang, and D. A. Muller, Nat. Mater. **5**, 204 (2006).

[21] K. Yoshimatsu, R. Yasuhara, H. Kumigashira, and M. Oshima, Phys. Rev. Lett. **101**, 026802 (2008).

[22] M. Sing, G. Berner, K. Goß, A. Müller, A. Ruff, A. Wetscherek, S. Thiel, J. Mannhart, S. A. Pauli, C. W. Schneider, P. R. Willmott, M. Gorgoi, F. Schäfers, and R. Claessen, Phys. Rev. Lett. **102**, 176805 (2009).

[23] W. Siemons, G. Koster, H. Yamamoto, W. A. Harrison, G. Lucovsky, T. H. Geballe, D. H. A. Blank, and M. R. Beasley, Phys. Rev. Lett. **98**, 196802 (2007).

[24] G. Herranz, M. Basletić, M. Bibes, C. Carrétéro, E. Tafra, E. Jacquet, K. Bouzehouane, C. Deranlot, A. Hamzić, J.-M. Broto, A. Barthélémy, and A. Fert, Phys. Rev. Lett. **98**, 216803 (2007).

[25] P. R. Willmott, S. A. Pauli, R. Herger, C. M. Schlepütz, D. Martoccia, B. D. Patterson, B. Delley, R. Clarke, D. Kumah, C. Cionca, and Y. Yacoby, Phys. Rev. Lett. **99**, 155502 (2007).

[26] V. K. Guduru, A. McCollam, A. Jost, S. Wenderich, H. Hilgenkamp, J. C. Maan, A. Brinkman, and U. Zeitler, Phys. Rev. B **88**, 241301 (2013).

[27] Z. S. Popovic, S. Satpathy, and R. M. Martin, Phys. Rev. Lett. **101**, 256801 (2008).

[28] S. Lerer, M. Ben Shalom, G. Deutscher, and Y. Dagan, Phys. Rev. B **84**, 075423 (2011).

[29] D. Rakhmilevitch, I. Neder, M. B. Shalom, A. Tsukernik, M. Karpovski, Y. Dagan, and A. Palevski, Phys. Rev. B **87**, 125409 (2013).

[30] S. S. A. Seo, Z. Marton, W. S. Choi, G. W. J. Hassink, D. H. A. Blank, H. Y. Hwang, T. W. Noh, T. Egami, and H. N. Lee, Appl. Phys. Lett. **95**, 082107 (2009).

[31] H. Y. Hwang, Y. Iwasa, M. Kawasaki, B. Keimer, N. Nagaosa, and Y. Tokura, Nat. Mater. **11**, 103 (2012).

[32] J. Mannhart and D. G. Schlom, Science **327**, 1607 (2010).

[33] I. Pallecchi, M. Codda, E. Galleani dAgliano, D. Marré, A. D. Caviglia, N. Reyren, S. Gariglio, and J.-M. Triscone, Phys. Rev. B **81**, 085414 (2010).

[34] A. Filippetti, P. Delugas, M. J. Verstraete, I. Pallecchi, A. Gadaleta, D. Marré, D. F. Li, S. Gariglio, and V. Fiorentini, Phys. Rev. B **86**, 195301 (2012).

[35] G. Koster, B. L. Kropman, G. J. H. M. Rijnders, D. H. A. Blank, and H. Rogalla, Appl. Phys. Lett. **73**, 2920 (1998).

[36] R. Fletcher, J. J. Harris, C. T. Foxon, M. Tsaousidou, and P. N. Butcher, Phys. Rev. B **50**, 14991 (1994).

[37] N. W. Ashcroft and N. D. Mermin, *Solid State Physics* (Harcourt College, Fort Worth, 1976).

[38] The data point at 7.5 K violates the Mott-Ioffe-Regel criterion ($k_f l < 1$). We still included it in the figure for completeness.

[39] M. J. Burns and P. M. Chaikin, J. Phys. C **18**, 743 (1985).

[40] For the thermoelectric tensor we can write, as explained below, $\epsilon_{xx} = \epsilon_{xx}^{(1)} + \epsilon_{xx}^{(2)}$. With $\epsilon_{xx}^{(i)} = \sigma_{xx}^{(i)} S_{xx}^{(i)}$ we get immediately $S_{xx}(\sigma_{xx}^{(1)} + \sigma_{xx}^{(2)}) = \sigma_{xx}^{(1)} S_{xx}^{(1)} + \sigma_{xx}^{(2)} S_{xx}^{(2)}$ and Eq. (2) follows.

[41] K. Behnia, J. Phys.: Condens. Matter **21**, 113101 (2009).

[42] S. Cao, R. Fletcher, M. Lakrimi, N. J. Mason, R. J. Nicholas, and P. J. Walker, Phys. Rev. B **54**, 5684 (1996).

[43] N. F. Mott and E. A. Davis, *Electronic Processes in Non-Crystalline Materials* (Clarendon, Oxford, 1971), p. 53.

[44] J. M. Ziman, *Electrons and Photons—The Theory of Transport Phenomena in Solids* (Clarendon, Oxford, 1960), p. 425.

[45] B. L. Gallagher and P. N. Butcher, in *Handbook on SemiConductors*, edited by P. Landsberg (Elsevier, Amsterdam, 1992), p. 728.

[46] R. Bel, K. Behnia, Y. Nakajima, K. Izawa, Y. Matsuda, H. Shishido, R. Settai, and Y. Onuki, Phys. Rev. Lett. **92**, 217002 (2004).

[47] M. Falkowski and A. Kowalczyk, J. Appl. Phys. **110**, 043709 (2011).

[48] R. Pentcheva and W. E. Pickett, Phys. Rev. Lett. **99**, 016802 (2007).